IJISET - International Journal of Innovative Science, Engineering & Technology, Vol. 12 Issue 08, August 2025
ISSN (Online) 2348 – 7968 | Impact Factor – 6.72
www.ijiset.com

Annealing-Induced Modifications in Nickel Phosphate Thin Films for Enhanced Supercapacitor Performance and Application Enrichment Using DFT Calculation

Supriya J. Shinde[a], Tanaji P. Gujar[b], Nandu B. Chaure[c] and Ramchandra T. Sapkal*[a]

[a]Department of Physics, Tuljaram Chaturchand College (Autonomous) Baramati, affiliated to Savitribai Phule Pune University (MS) India 413102

[b]Department of Physics, ADT's Shardabai Pawar Mahila Art's, Commerce and Science College, Sharda Nagar, Baramati, (MS), India 413115.

[c]Department of Physics, Savitribai Phule Pune University Ganesh Khind, Pune University Campus, Pune, (MS), India 411007

*Corresponding Author – Dr. Ramchandra T. Sapkal: sapkalramchandra33@gmail.com

Supriya J. Shinde: sjshinde555@gmail.com

Abstract

Nickel phosphate ($Ni_3(PO_4)_2$) is considered a promising candidate for energy storage applications owing to its multiple valence states that enhance charge transfer, high theoretical specific capacitance, and versatile redox characteristics. The present study investigates the influence of thermally induced changes in crystallinity on the electrochemical performance of $Ni_3(PO_4)_2$ thin films for supercapacitor applications. Controlled annealing at 350 °C for one hour resulted in notable alterations in the structural and morphological properties of the films, thereby improving their charge storage capacity and cyclic stability. Structural analysis confirmed the transition from near amorphous to more crystalline phases, which facilitated improved electron and ion transport. Electrochemical analysis revealed a significant enhancement in specific capacitance, rate capability, and overall energy storage efficiency following thermal treatment. A maximum specific capacitance of 1191 F g^{-1} was achieved post-annealing. The specific capacitance and cyclic stability exhibited superior performance compared to previously reported values. The density functional theory calculations were carried out using quantum espresso packs to verify experimental values.

Keywords: *Nickel phosphate, Structural modifications, Surface modification, Binder-free synthesis, Symmetric Supercapacitor*

Introduction:

Now a day's world population increases in large amount. As population increases the energy demand is also increases. Energy storage devices designed for high-power applications have garnered considerable research interest due to the escalating global energy demands. Consequently, the primary objective is to develop systems capable of not only efficient and reversible energy storage but also rapid delivery of electrical energy. This can be achieved through the use of supercapacitor (SC) devices [1, 2]. The mechanism of charge storage classifies supercapacitors into electrochemical double layer capacitor (EDLCs), pseudo- capacitors, and hybrids [3]. To meet energy storage requirements, researchers have developed and studied numerous materials for supercapacitor (SC) applications, including transition metal oxides [4], hydroxides [5], sulphides [6], carbides and phosphides [7]. Despite their potential, these materials suffer from drawbacks such as inadequate stability, limited conductivity, and lower specific capacitance [8, 9]. Addressing high energy and cost-efficiency requirements calls for the improvement of electrode materials with low cost, high specific

capacitance, and good cycling performance [10]. Extensively investigated over the years, transition metal phosphates have found applications in areas like Energy storage devices [11] and sensors [12], catalysis and photocatalysis [13,14,15]. In recent times, their application in energy storage has gained momentum, driven by their excellent electrical properties, ample active sites, open-channel structures for rapid ion diffusion, and structural robustness arising from strong phosphorus–oxygen covalent bonding [16]. $Ni_3(PO_4)_2$ is recognized for its impressive electrochemical activity and environmental sustainability. Still, its efficiency is strongly dependent on its morphology and structure, which control the movement of ions and flow of electrons. The ionic conductivity and rate capability of nickel phosphates can vary based on their structure, such as pyrophosphate or orthophosphate forms [17]. Developing economically viable and stable materials with high energy and power densities for supercapacitors requires the discovery of new material systems. Transition metal phosphates have emerged as attractive candidates for such applications due to their promising electrochemical characteristics [18]. Recent research efforts have been directed toward enhancing the performance of $Ni_3(PO_4)_2$-based electrodes by optimizing synthesis techniques, developing hybrid composites (such as $Ni_3(PO_4)_2$ integrated with carbon materials or metal oxides), and improving electrolyte compatibility. These approaches are designed to develop high-efficiency, affordable supercapacitors that can be employed in diverse applications such as energy storage systems, portable electronics, and electric vehicles. $Ni_3(PO_4)_2$-based composites exhibit enhanced specific capacitance, improved charge transport, and excellent cycling durability, making them ideal candidates for future supercapacitor electrodes.

In this work, a cost-effective and reproducible chemical bath deposition (CBD) method was used to synthesize $Ni_3(PO_4)_2$ electrode material. The influence of annealing on the structural and morphological properties of the prepared electrodes was systematically investigated by varying the calcination temperature. Furthermore, the effect of these structural and morphological changes on the electrochemical activity of the supercapacitors was thoroughly examined through the experimentally and first principle method. To investigate the electronic structure of $Ni_3(PO_4)_2$ and evaluate the reliability of the experimental approach, we employed first-principles calculations based on Density Functional Theory (DFT). The outcomes of these theoretical calculations provide valuable guidance for designing a rational experimental strategy. The combination of experimental and theoretical insights contributes to a deeper understanding and more efficient development of nanomaterials for energy storage applications.

2.Experimental

2.1. Materials and methods

Source of nickel from nickel nitrate hexahydrate (Ni $(NO_3)_2.6H_2O$), source of phosphate from potassium dihydrogen orthophosphate (KH_2PO_4) and ammonia as complexing agent. All chemicals are purchased from Loba Chemicals (AR grade) and used without any purification. Simple CBD method was used to synthesis the thin film of, $Ni_3(PO_4)_2$ on stainless steel (SS) substrate. 50 ml of precursor solution, 0.075 M Ni $(NO_3)_2.6H_2O$ and 0.05 M KH_2PO_4 were separately mixed in double distilled water. Thin film samples were prepared to study the annealing effect of prepared electrode material of nickel phosphate with same molar concentration of (Ni $(NO_3)_2.6H_2O$), and (KH_2PO_4). Cleaned glass and SS substrates were kept at constant temperature 338K for 4 hrs. During the precipitation, heterogeneous reaction occurred on the substrate and the deposition of nickel phosphate took place on the substrate surface.

As-deposited and air-annealed (623^0K) $Ni_3(PO_4)_2$ thin films were thoroughly characterized and applied as cathode materials in supercapacitor devices. Structural analysis of the prepared material was performed by XRD using a Rigaku Miniflex-600 diffractometer and CuK_α radiation (λ = 0.15425 nm). FT–IR spectra, recorded with a Bruker Alpha II instrument, were used to identify the functional groups. Morphological features were examined through FE-SEM (JSM-7001F, JEOL). Electrochemical activities measured using admiral squid stat electrochemical workstation. Electrochemical measurements for both as-deposited and annealed ($Ni_3(PO_4)_2$) thin films were performed on an admiral squid stat electrochemical workstation. Electrochemical measurements were conducted using a three-electrode setup comprising a $Ni_3(PO_4)_2$ thin film (working electrode), platinum plate (counter electrode), and saturated calomel electrode (SCE) (reference electrode). CV and GCD techniques were employed at room temperature to assess the supercapacitor characteristics.

Density functional theory (DFT) is calculated for ($Ni_3(PO_4)_2$) using Quantum Espresso packs to variable experimental values. Not only the DFT but also, the partial density of states (PDOS) studied using the graphical data representation. The quantum confinement effect and density of states responsible to contribute quantum capacitance (QC) of 2D materials [19].

2.2 Computational Methodology

First-principles calculations were performed within the framework of DFT as implemented in the Quantum ESPRESSO package, version 7.4.1. The exchange–correlation interactions were treated using the generalized gradient approximation (GGA) parameterized by the Perdew–Burke–Ernzerhof revised for solids (PBEsol) functional [20, 21]. The electron–ion interactions were described by projector augmented-wave (PAW) and ultrasoft pseudopotentials obtained from the PSL and pslibrary repositories [22]. A kinetic energy cutoff of 50 Ry for the plane-wave basis set and 400 Ry for the charge density was employed, ensuring adequate convergence of the total energy. A spin-polarized calculation was performed with an initial ferromagnetic ordering to account for possible magnetic interactions of the Ni 3d orbitals. If required, the on-site Coulomb interactions for the Ni 3d states were incorporated within the DFT+U framework using a Hubbard U parameter of 6 eV [23,24]. The Brillouin zone was sampled using a Monk horst-Pack k-point mesh of 9×8×5 for the self-consistent field (SCF) calculation, were converged with a threshold of 5×10^{-9} Ry for the total energy. The structural parameters were optimized until the forces on each atom were less than 1×10^{-4} Ry/Bohr. The density of states (DOS) and projected density of states (PDOS) were calculated using a denser k-point grid (e.g., 12×12×12), and the tetrahedron method with Bloch corrections [25].

3. Results and discussion

3.1. Synthesis of $Ni_3(PO_4)_2$ thin film

In the CBD method, once the solution reaches a supersaturated state, ionic species begin to adsorb onto the surface of the substrate, initiating nucleation through a heterogeneous reaction. This is followed by a continuous growth process, leading to the formation of the thin film. During the reaction, Ni^{2+} ions released from Ni $(NO_3)_2\cdot6H_2O$ interact with ammonia to form a nickel-ammonia complex, $[Ni\ (NH_3)]^{2+}$, which serves as a controlled source of nickel ions, thereby regulating the reaction kinetics. The PO_4^{3-} ions released from KH_2PO_4 dissociation react with Ni^{2+} ions in solution to form $Ni_3(PO_4)_2$, which deposits as a thin film over the SS substrate. A reaction time of 4 hours was found to be optimal for forming a well-adherent, apple green nickel phosphate thin film on the SS substrate. The amount of material deposited was determined using the gravimetric method by measuring the weight difference method of the substrate before and after deposition.

3.2. XRD Analysis

The XRD patterns of the as-deposited and annealed $Ni_3(PO_4)_2$ films are shown in Fig.1. Distinct diffraction peaks corresponding to *d*-spacings of 5.59, 3.23, and 2.93 Å are observed, which are indexed to the (110), ($\bar{2}$11), and (122) crystallographic planes, respectively. Additional peaks marked with an asterisk (*) are attributed to the SS substrate. The diffraction patterns of both film types closely matched with the standard JCPDS card no. 00-049-1082, confirming the successful formation of $Ni_3(PO_4)_2$ on the SS substrate.

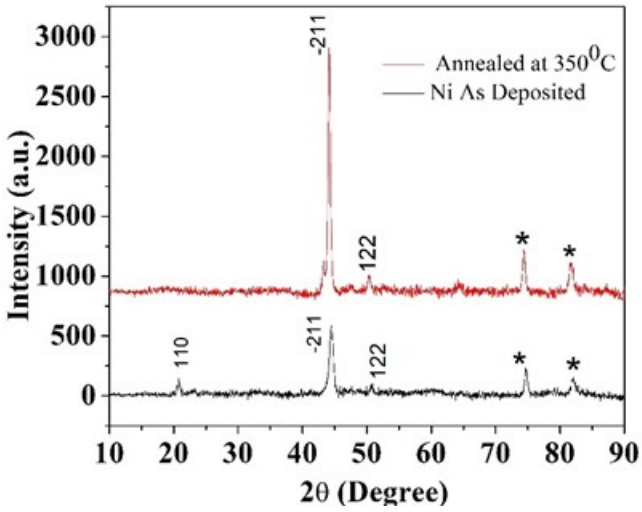

Fig.1. XRD of as-deposited and annealed $Ni_3(PO_4)_2$ thin film

The FTIR spectra shown in Fig.2 illustrate the vibrational stretching modes of chemical bonds in nickel-based thin films before and after annealing at 623K. In the lower wavenumber region (520–620 cm^{-1}), distinct absorption bands are observed corresponding to the Ni–O stretching vibrations, which are more prominent in the annealed sample, indicating enhanced formation or ordering of nickel-oxygen bonds due to thermal treatment [26]. Peak observed in the range of 1000–1200 cm^{-1}, with distinct features, corresponds to the asymmetric and symmetric stretching vibrations of P–O bonds, which are characteristic of phosphate (PO_4^{3-}) groups [27,28]. These peaks are observed in both samples but become more well-defined after annealing. Additionally, a broad absorption band around 3200–3600 cm^{-1} is observed in the as-deposited film, which corresponds to the O–H stretching vibrations from hydroxyl groups or adsorbed water molecules. This O–H stretching band significantly diminishes after annealing, indicating the removal of moisture or hydroxyls upon heating, resulting in a more compact and chemically stable thin film.

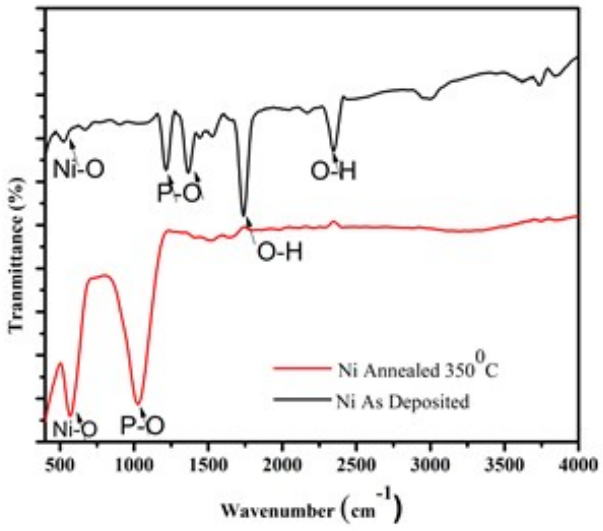

Fig.2. FTIR of $Ni_3(PO_4)_2$ thin film electrode

3.3. Morphological Analysis

The surface morphology of $Ni_3(PO_4)_2$ thin films of as-deposited and annealed conditions studied by scanning electron microscopy (SEM) images (Fig.3). The as-deposited film displays a highly porous, sponge-like network formed by uniformly agglomerated nanoparticles. After annealing, the nanostructure appears shrunken and more compact (Fig.3a and b), likely due to the removal of hydroxide components, which may trigger grain bursting [29]. The film shows good surface coverage without visible cracks or peeling, indicating a uniform deposition and mechanical stability, which are important for ensuring long-term cycling performance in energy storage devices. The nano-porosity and interconnected particle network are beneficial for fast ion diffusion and efficient electron transport, which directly influence the capacitive performance.

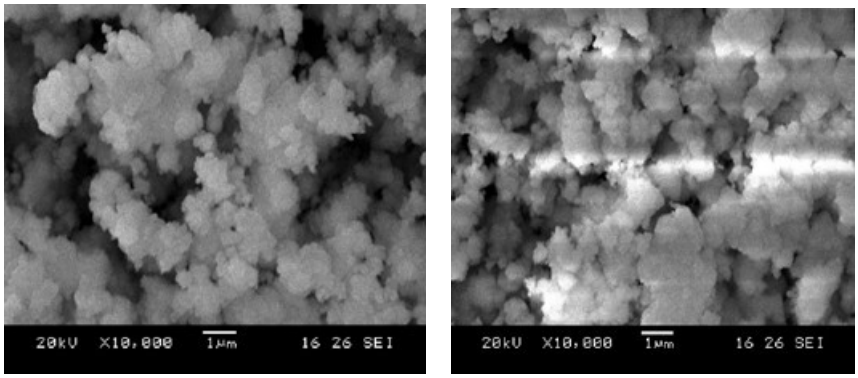

Fig.3.SEM of (a) As – Deposited and (b) Annealed $Ni_3(PO_4)_2$ thin films

3.4. Density Functional Theory (DFT) Analysis

Local Density Approximation LDA tends to overestimate binding energies and performs poorly for systems with strongly localized electrons, such as *d*- and *f*-block elements. To address these limitations, the Generalized Gradient Approximation (GGA) was developed. GGA functionals, such as PW91 and Perdew–Becke–Ernzerhof (PBE) [30], consider both the local electron density and its gradient, leading to improved accuracy for a wider range of materials. The total density of states (TDOS), which plays important role in DFT calculations. TDOS plots provide valuable insights into the electronic structure of a material, revealing details such as the bandgap, bonding characteristics, hybridization, doping effects, metallic behaviour, and magnetic properties. In spin-polarized systems, TDOS can differentiate between spin-up and spin-down states, with any asymmetry between them indicating magnetic behaviour. A higher TDOS value generally implies better electrical conductivity. In the context of supercapacitor simulations, TDOS is particularly important for determining the quantum capacitance (C_Q), which is derived from the DOS using the following expression:

$$C_Q = e^2 \int D(E)\, F_T\left(E - e_{\varphi_G}\right) dx \qquad (1)$$

where, e represents the electronic charge, $D(E)$ is the density of states, E denotes the energy, ϕ_G is the electrode potential, and $F_T(E)$ is the thermal broadening function. From this expression, it is evident that the quantum capacitance (C_Q) is directly related to the DOS near the Fermi level.

DFT theory states that are significantly distant from the fermi energy contribute minimally C_Q.
The thermal broadening function $F_T(E)$ is defined as:

$$F_T(E) = (4K_BT)^{-1} sh^2\left(\frac{E}{2KBT}\right) \qquad (2)$$

Where, K_B is the Boltzmann constant and T is the temperature.

The total capacitance is calculated by the formula [31],

$$\frac{1}{\mathrm{Cr}} = \frac{1}{\mathrm{CQ}} + \frac{1}{C_{EDL}} \quad (3)$$

C_{EDL}- electric double-layer capacitance. It influenced by the nature of the electrode–electrolyte interface.

The electronic band structure and DOS (Fig.4) of nickel phosphate $Ni_3(PO_4)_2$, calculated using DFT. The band structure is plotted along high-symmetry points in the Brillouin zone (Γ–Z–D–B–Γ–A–E–Z–C_2–Y_2–Γ), while the DOS is shown on the right side of the plot. $E - E_f$ is set at 0 eV (Fig.4), where the E_f is the fermi energy. From the band structure, it is evident that $Ni_3(PO_4)_2$ exhibits a finite band gap (3.6 eV), suggesting its semiconducting behaviour. The band edges (red dots) occur at different k-points, showing a direct gap. The corresponding DOS plot confirms it is characteristic of semiconductors. In the context of quantum capacitance and supercapacitor applications, this band gap plays a significant role. The quantum capacitance is directly related to the DOS at the fermi level; in semiconductors like $Ni_3(PO_4)_2$, tuning the Fermi level can effectively modulate the carrier concentration and enhance the electrochemical response. The sharp increase in DOS near the conduction and valence band edges can contribute to charge storage capacity, especially when the material operates in a pseudocapacitive regime.

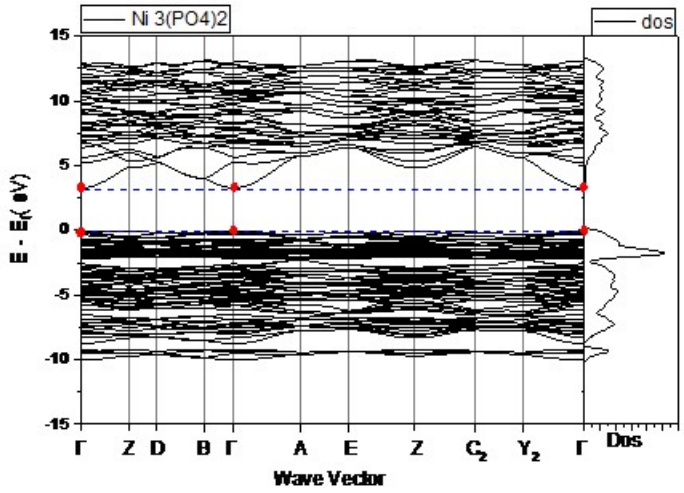

Fig.4. Electronic band structure and density of states (DOS) of $Ni_3(PO_4)_2$

The electronic configuration of Ni:$1s^2 2s^2 2p^6 3s^2 3p^6 3d^8 4s^2$, O: $1s^2 2s^2 2p^4$ and P: $1s^2 2s^2 2p^6 3s^2 3p^3$.The partial density of states (PDOS) of $Ni_3(PO_4)_2$ (Fig.5), which provides detailed insight into the elemental and orbital contributions to the electronic structure of the material. PDOS analysis is particularly significant for understanding quantum capacitance behaviour in supercapacitor applications, as it identifies the orbitals and atoms actively participating in charge storage near the Fermi level. The totals PDOS (Fig.5. (a)) is decomposed into contributions from Ni, P, and O atoms, with a prominent peak near the Fermi level ($E - E_f = 0$ *eV*) mainly contributed by oxygen (O) states, followed by nickel (Ni). This suggests that oxygen orbitals play a dominant role in the electronic activity around the Fermi level, which is crucial for electrochemical charge transfer processes. Further resolves (Fig.5. (b)) the nickel orbitals, showing that the Ni *3d* orbitals significantly contribute near the Fermi level, indicating their key role in electronic conductivity and possibly redox activity both critical for pseudocapacitive behaviour. The contribution of Ni *1s*, *2s*, and *2p* orbitals is minor in this energy range. The PDOS (Fig.5. (c)) for phosphate (P) shows that P *3p* orbitals are primarily active at higher energies (band gap = 3.6 eV), while P *1s* and *2p* have negligible contributions near the Fermi level. This implies that phosphorus contributes mainly to the deeper valence bands and does not directly affect charge storage near the Fermi level. The oxygen (Fig.5. (d)) orbitals, where O *2p* states dominate the valence band just below the Fermi level. These states are responsible for strong hybridization with Ni *3d* orbitals, facilitating electronic transitions that enhance quantum capacitance the ability of the electrode to accumulate charge depending on the electronic DOS at the Fermi level. The PDOS analysis of $Ni_3(PO_4)_2$ highlights that the Ni *3d* and O *2p* orbitals are the primary contributors to the DOS near the Fermi level, making them critical for improving the quantum capacitance. This characteristic enhances the electrochemical performance of $Ni_3(PO_4)_2$ as an electrode material for supercapacitor applications, where efficient charge transfer and high electronic activity are essential.

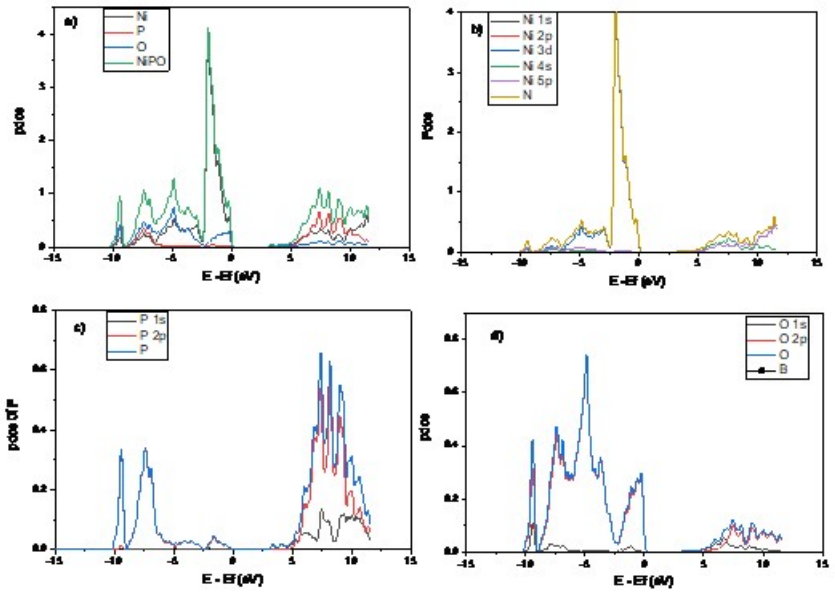

Fig.5. Partial Density States (PDOS) of $Ni_3(PO_4)_2$

3.5. Electrochemical Analysis of $Ni_3(PO_4)_2$

Cyclic Voltammetry (CV) was employed to evaluate the electrochemical properties of the $Ni_3(PO_4)_2$ electrode across scan rates from 5 to 50 mV s^{-1}. The CV curves (Fig.6) exhibit a quasi-rectangular shape, indicative of pseudocapacitive behaviour and swift, reversible redox reactions. At a scan rate of 5 mV/s, sharp and well-defined redox peaks are visible, pointing to favourable ion mobility within the electrode material. As the scan rate rises, the peaks widen and shift, highlighting the impact of reduced diffusion time on reaction kinetics. Although peak broadening occurs at higher scan rates, the overall CV curve shape remains stable, suggesting that the $Ni_3(PO_4)_2$ electrode maintains excellent electrochemical performance and rate capability. As the scan rate increases, a steady rise in peak current is observed, confirming its capacitive characteristics and potential for advanced supercapacitor applications. The linear correlation between voltametric current and scan rate further affirms its ideal capacitive nature. However, the specific capacitance decreases significantly from 1191 F g^{-1} at 5 mV $s^{-1}$to 74.62 F g^{-1} at 50 mV s^{-1} likely due to insufficient time for ions to penetrate deeper active sites, resulting in incomplete redox activity at higher scan rates.

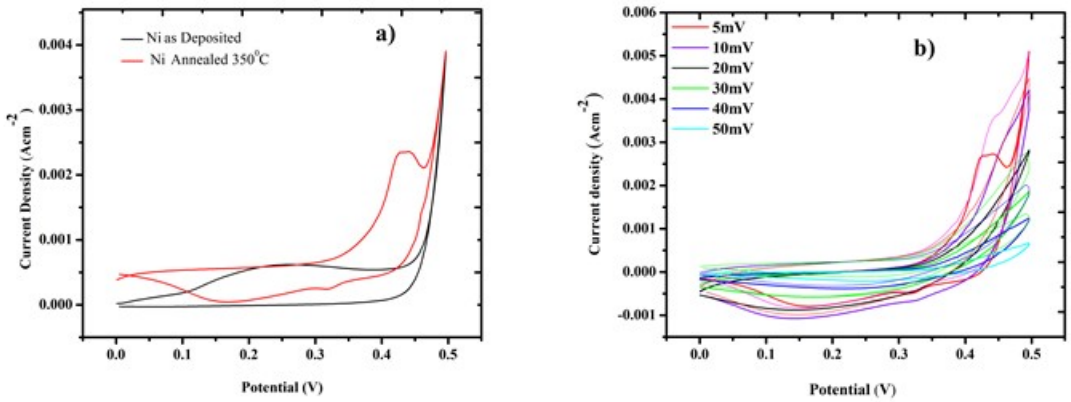

Fig.6.a) CV curve of 5 *mV* s^{-1} scan rate for as -deposited and annealed $Ni_3(PO_4)_2$ thin films, **b)** CV curves for annealed $Ni_3(PO_4)_2$ sample for different scan rate.

$Ni_3(PO_4)_2$ electrodes were subjected to GCD measurements in the voltage range of 0–0.5 V at a current density of 0.5 mA cm^{-2} to examine their charge–discharge behaviour (Fig.7). The resulting voltage–time plots reveal a non-symmetric profile, featuring a noticeable IR drop, which points to internal resistance in the system. The discharge segment typically displays two features: a steep initial voltage drops, nearly parallel to the *y*-axis, indicating resistance effects, followed by a curved region corresponding to the capacitive response of the electrode.

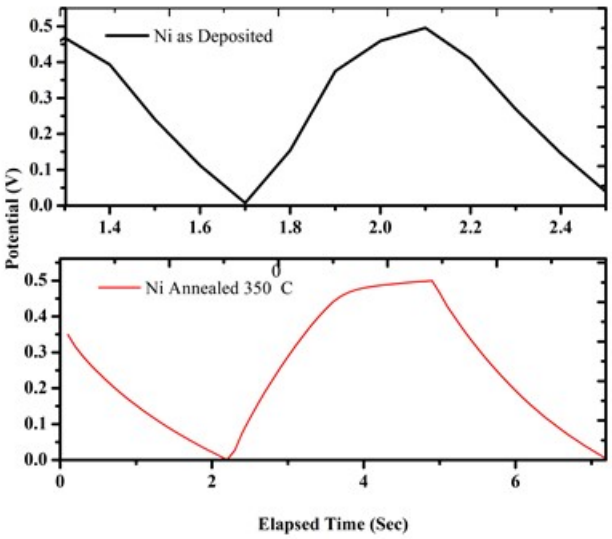

Fig.7.GCD of as –deposited and annealed $Ni_3(PO_4)_2$ thin film electrodes

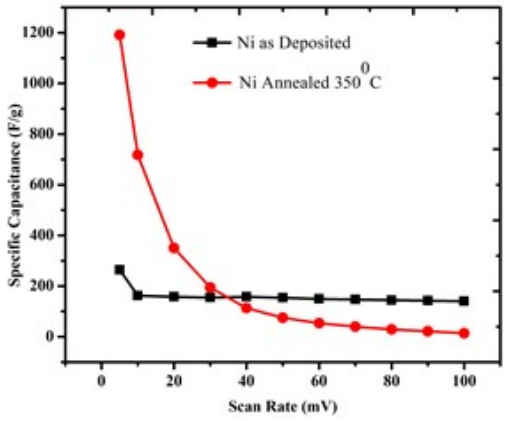

Fig.8. Specific Capacitance Vs Scan rate for as - deposited and annealed $Ni_3(PO_4)_2$ thin films.

Specific Capacitance verses scan rate for as deposited and annealed $Ni_3(PO_4)_2$ thin films shown in (Fig.8).This graph typically shows a decreasing trend. At lower scan rates, electrolyte ions have more time to diffuse into the inner pores of the electrode material, leading to higher charge storage and, consequently, higher specific capacitance [32]. As the scan rate increases, the ion diffusion becomes limited to the outer surface of the electrode due to insufficient time, resulting in lower specific capacitance. This behaviour is indicative of pseudo-capacitive or battery-type behaviour in nickel phosphate, where redox reactions contribute significantly to charge storage [33]. The shape of the curve and the retention of capacitance at high scan rates also give insight into the rate capability and overall performance of the electrode material. When plotted, the graph of specific capacitance versus scan rate typically shows a decreasing trend.

4. Conclusions

$Ni_3(PO_4)_2$ thin films exhibiting near crystalline phase were successfully synthesized via a simple CBD technique. XRD and FTIR analysis confirmed the formation of $Ni_3(PO_4)_2$. SEM images revealed that the as-deposited films possessed a highly porous, sponge-like nanostructure composed of uniformly distributed, agglomerated nanoparticles, which became denser upon annealing. Electrochemical measurements demonstrated that the amorphous $Ni_3(PO_4)_2$ exhibited superior performance compared to its crystalline counterpart. The highest specific capacitance of 1191 F g^{-1} was recorded for the annealed, near-crystalline $Ni_3(PO_4)_2$ thin film electrode. The quantum capacitance of $Ni_3(PO_4)_2$, derived from the density of states (DOS) near the Fermi level, shows a peak value of 452 Fg^{-1}, indicating substantial electronic states available for charge accumulation. The PDOS confirms Ni *3d* and O *2p* orbital contributions near the Fermi level, enhancing the charge storage capability.

Author contributions

All authors contributed to the study conception and design. Material preparation, data collection, and analysis were performed by Supriya J. Shinde. The first draft of the manuscript was written by Supriya J. Shinde and supervision was performed by Tanaji P. Gujar, Nandu B. Chaure and Ramchandra T. Sapkal. All authors commented on previous versions of the manuscript. All authors read and approved the final manuscript.

Acknowledgment

SJS sincerely acknowledges the financial assistance provided under the SARTHI Fellowship by the Chhatrapati Shahu Maharaj Research, Training and Human Development Institute (SARTHI), Government of Maharashtra, India. DST, FIST and Principal of Tuljaram Chaturchand College providing research facilities.

Declarations

Conflict of interest

The authors declare that they have no known competing financial interests or personal relationships that could have appeared to influence the work reported in this paper.

Informed consent

Not applicable.

Research Data Policy

Standardized methods are used for research data collection, accurate documentation with scientific ethics.

Data availability

Data will be made available on reasonable request.

Research involving human participants and/or animals

This research did not involve any studies with human participants or animals performed by any of the authors.

Acknowledgment

SJS sincerely acknowledges the financial assistance provided under the SARTHI Fellowship by the Chhatrapati Shahu Maharaj Research, Training and Human Development Institute (SARTHI), Government of Maharashtra, India. DST, FIST and Principal of Tuljaram Chaturchand college providing research facilities.

References

[1] Y. Shao, M. El-Kady, J. Sun, Y. Li, Q. Zhang, M. Zhu, H. Wang, B. Dunn, R. Kaner, *Chem. Rev*. 118,9233–9280 (2018).

[2] U. Patil, M. Nam, J. Sohn, S. Kulkarni, R. Shin, S. Kang, S. Lee, J. Kim, S. Jun, *J. Mater. Chem. A* 2, 19075–19083 (2014).

[3] M. Vangari, T. Pryor, L. Jiang, *J. Energy Eng.* 139, 72–79 (2013).

[4] U. Patil, S. Kulkarni, V. Jamadade, C. Lokhande, *J. Alloy Comp.* 509, 1677–1682 (2011).

[5] U. Patil, K.Gurav, J.Kim, C. Lokhande, S. Jun, *Bull. Mater. Sci.* 37, 27–33 (2014).

[6] X. Yu, L. Yu, H. Wu, X. Lou, *Angew. Chem. Int. Ed.* 54, 5331–5335 (2015).

[7] S. Liu, K. Sankar, A. Kundu, M. Ma, J. Kwon, S. Jun, A.C.S. *Appl, Mater. Interfaces* 9, (1838) 21829–21832 (2017).

[8] F. Shi, L. Li, X. Wang, C. Gu, J. Tu, *RSC Adv.* 4, 41910–41921 (2014).

[9] G. Snook, P. Kao, A. Best, *J. Power Sources* 196,1–12 (2011).

[10] C. Chen, N. Zhang, Y. He, B. Liang, R. Ma, X. Liu, *ACS Appl. Mater. Interfaces* 8, 23114–23121 (2016).

[11] B. Li, P. Gu, Y. Feng, G. Zhang, K. Huang, H. Xue, H. Pang, *Adv. Funct. Mater* 27, 1605784–1605795 (2017).

[12] S. Darzi, M. Esfidvajani, *J. Porous Mater.* 24, 24,85–95, 2017.

[13] R. Pujari, V. Lokhande, V. Kumbhar, N. Chodankar, C. Lokhande, *J Mater Sci: Mater Electron 3312-3317, (2016).*

[14] S. Marje, P. Katkar, S. Kale, A. Lokhande, C. Lokhande, U. Patil, *J. Alloys Compd*. 779, 49–58 (2019).

[15] Y. Bi, S. Ouyang, N. Umezawa, J. Cao, J. Ye, *J. Am. Chem. Soc.* 133, 6490–6492 (2011).

[16] X. Li, A. Elshahawy, C. Guan, J. Wang, *Small* 13, ,1701530–1701554, (2017).

[17] H. Pang, X. Li, X. Xiao, Q. Li, J. Wei, H. Xue, *Inorg. Chem. Front.* 5, 11–28, (2018).

[18] M. Vangari, T. Pryor, L. Jiang, *J. Energy Eng.* 139, 72–79, (2013).

[19] G. Yang, X. Yang, Z. Li, H. Huang and J. Lin, *RSC Adv.*13, 2779 2-27800, (2023).

[20] P. Giannozzi et al., *J. Phys.: Condens. Matter* 21, 395502 (2009).

[21] J.P. Perdew et al., *Phys. Rev. Lett.*100, 136406 (2008).

[22] A. Corso, Comput. *Mater. Sci.* 95, 337–350 (2014).

[23] V. Anisimov et al., *Phys. Rev.* 44, 943 (1991).

[24] M. Cococcioni and S.de Gironcoli, *Phys. Rev.* 71, 035105 (2005).

[25] P.E. Blöchl, O. Jepsen, O.K. Andersen, *Phys. Rev.* 49, 16223 (1994).

[26] X. Qiang, S. Xue, S.Wei-Han, Y. Guang-Min. *Acta Phys. Sin.*, 70, 107301 (2021).

[27] S. Navale, V. Mali, S. Pawar, R. Mane, M. Naushad, F. Stadler, V. Patil, *RSC Adv.* 5, 51961–51965 (2015).

[28] M. Al-Omair, A. Touny, M. Saleh, *J. Power Sources* 342,1032–1039 (2017).

[29] D. Yang, Q. Yu, L. Gao, L. Mao, J. Yang, *Appl. Surf. Sci.* 416, 503–510 (2017).

[30] J.P. Perdew, K. Burke, M. Ernzerhof, *Phys. Rev. Lett.* 77, 3865 – 3868 (1995).

[31] R. Samal, S. Mondal, A.S. Gangan, B. Chakraborty, C.S. Rout, *Phys. Chem. Chem. Phys.* 22, 7903-7911 (2020).

[32] G. Wang, L. Zhang and J. Zhang, *Chem. Soc. Rev.* 41, 797–828 (2012).

[33] G. A. M. Ali, S. A. B.A. Manaf, A. Kumar, K. F Chong and G. Hegde, *J. Phys. D: Appl. Phys.* 47, 495307 (2014)